ACS APPLIED MATERIALS & INTERFACES

Research Article

www.acsami.org

AlOOH-Reduced Graphene Oxide Nanocomposites: One-Pot Hydrothermal Synthesis and Their Enhanced Electrochemical Activity for Heavy Metal Ions

Chao Gao,[†,‡,§] Xin-Yao Yu,[‡,§] Ren-Xia Xu,[†,‡] Jin-Huai Liu,[‡] and Xing-Jiu Huang*[,†,‡]

[†]Department of Chemistry, University of Science and Technology of China, Hefei 230026, P.R. China

[‡]Research Center for Biomimetic Functional Materials and Sensing Devices, Institute of Intelligent Machines, Chinese Academy of Sciences, Hefei 230031, P.R. China

Supporting Information

ABSTRACT: This work described the preparation, characterization, and electrochemical behavior toward heavy metal ions of the AlOOH-reduced graphene oxide nanocomposites. This new material was synthesized through a green one-pot hydrothermal method. The morphologic and structure of the nanocomposites were characterized using atomic force microscopy, X-ray diffraction, Raman spectroscopy, X-ray photoemission spectroscopy, Fourier transform-infrared spectroscopy, and transmission electron microscopy. Electrochemical properties were characterized by cyclic voltammetry and electrochemical impedance spectroscopy. The chemical and electrochemical parameters that have influence on deposition and stripping of metal ions, such as pH value, deposition potential, and deposition time, were also studied. Due to the strong affinity of AlOOH to heavy metal ions and the fast electron-transfer kinetics of graphene, the combination of solid-phase extraction and stripping voltammetric analysis allowed fast and sensitive determination of Cd(II) and Pb(II) in drinking water, making these new nanocomposites promising candidates for practical applications in the fields of detecting heavy metal ions. Most importantly, these new nanocomposites may possess many unknown properties waiting to be explored.

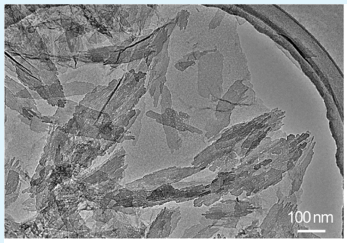

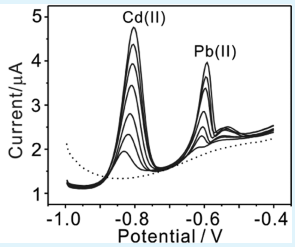

KEYWORDS: *AlOOH, reduced graphene oxide, nanocomposites, hydrothermal synthesis, electrochemical activity, heavy metal ions*

1. INTRODUCTION

The rapid, sensitive, and simple determination of trace heavy metal ions is of concern in the biosphere due to their high toxicity to human health. Because of the dependence on ponderous and complicated instruments, the commonly used spectrometric methods for the analysis of heavy metal ions are expensive and not suitable for the in situ analysis. However, the electrochemical method, as an alternative to these spectroscopic techniques, has been accepted as an efficient method to detect heavy metal ions due to their excellent sensitivity, short analysis time, portability, and low cost.[1] Usually, mercury based electrodes such as hanging drop mercury electrode and mercury film electrode are adopted because of excellent reproducibility and high-sensitivity.[2,3] However, general concerns about mercury toxicity still lead to an extensive search for new electrode materials.

Solid-phase extraction (SPE) is a popular sample preparation method and is very actively used in the field of separation science. There have already been many reports for the use of SPE in determination of heavy metal ions based on the spectrometric method[4−8] and determination of organic compounds based on the electrochemical method.[9−12] Thus, we try to introduce the idea of SPE into electrochemical detection of heavy metal ions. The efficient preconcentration of toxic metal ions onto a certain substrate is significant in stripping analysis. Stripping voltammetry combined with SPE will obviously meet the requirements of field detections of heavy metal ions well with high sensitivity. Therefore, it is important to find a proper and efficient SPE sorbent to modify the electrode surface for adsorbing toxic metal ions. Widespread attention has been paid to the nanomaterials due to their unique properties, which make them suitable for application as SPE sorbents.[6,13] In recent reports, γ-AlOOH was found to have a high adsorption capacity toward Cd(II) and Pb(II).[14−16] Thus, we try to use γ-AlOOH as solid-phase extraction sorbents to modify the electrode surface for detecting Cd(II) and Pb(II). However, as is well-known, metal oxides usually do not provide a good electrical conductivity, which inhibit their electrochemical activity. Therefore, one needs to find a good carrier which can provide the necessary conduction pathways for electrons on the electrode surface.

Graphene, as a "star" material, has been widely employed as an advanced substrate and conducting pathway for constructing

Received: June 10, 2012
Accepted: August 27, 2012
Published: August 27, 2012

electrochemical sensors. Compared with other carbon nanomaterials in electrochemical detection of heavy metal ions, such as carbon nanotubes,[17,18] mesoporous carbon,[19] graphite nanofibers,[20] and heated graphite nanoparticles,[21] graphene can have better performance owing to its extraordinary electronic transport properties, large surface area, and high electrocatalytic activities.[22,23] Most of graphene used in electrochemistry is produced from the reduction of graphene oxide (GO). However, because of the van der Waals and $\pi-\pi$ stacking interactions among individual graphene sheet interactions, the as-reduced graphene oxide (RGO) sheets tend to form irreversible agglomerates and even restack to form graphite.[24−26] By incorporation of nanomaterials into graphene sheets, the aggregation problem of graphene sheets could be minimized or prevented.[27] Inspired by this idea, many graphene-supported nanocomposites have been fabricated, aiming to employ them in electrochemical detection of heavy metal ions, such as graphene decorated with metal nanoparticles[28] and conducting polymer.[29,30] However, very few reports on graphene decorated with metal oxides could be found in electrochemical detection of heavy metal ions. Moreover, we found that graphene anchored with AlOOH has never been reported.

In this work, we tried to combine the high adsorption capacity of γ-AlOOH with the conductivity of graphene to fabricate an electrochemical platform for the simultaneous analysis of Cd(II) and Pb(II) in solution by square wave anodic stripping voltammograms (SWASV) for the first time. This new material of AlOOH-RGO nanocomposites have been successfully synthesized through a simple one-pot hydrothermal method. Under the hydrothermal condition, GO is simultaneously reduced to graphene along with the homogeneous precipitation of AlOOH nanoplates. Herein, the AlOOH nanoplates prevented the graphene from gathering together, and the RGO provided conducting pathways for improving electron transport on modified electrode surfaces. Additionally, ascribed to the involvement of AlOOH nanoplates homogeneously dispersed on RGO, it help to accumulate the target heavy metal ions on the electrode surface. Thus, the AlOOH-RGO nanocomposite modified glass carbon electrode showed enhanced sensing performance compared with single AlOOH and single graphene. On the basis of this work, we prove the new bridge between adsorption and electrochemical behavior.

2. EXPERIMENTAL SECTION

2.1. Chemical Reagents. Graphite (325 mesh) was from Alfa Aesar; all other reagents were commercially available from Sinopharm Chemical Reagent Co., Ltd. (China) with analytical grade and were used without further purification. Acetate buffer solutions of 0.1 M for different pHs were prepared by mixing stock solutions of 0.1 M NaAc and HAc. The water (18.2 MΩ cm) used to prepare all solutions was purified with the NANOpureDiamond UV water system.

2.2. Preparation of AlOOH-Reduced Graphene Oxide Nanocomposites. Graphene oxide was prepared from natural graphite by a modified Hummers' method.[31] Then, the AlOOH-RGO nanocomposites were synthesized as in the following procedure by a one-pot hydrothermal method. Namely, 0.57 g of $Al(NO_3)_3{\cdot}9H_2O$ and 0.27 g of urea were added to 18 mL of 0.5 mg·mL^{-1} GO aqueous solution under stirring. The above mixture was sonicated at 25 °C for 30 min, and then, it was transferred and sealed into a 23 mL Teflon-lined stainless steel autoclave, heated at 180 °C in an electric oven for 10 h, and then cooled to room temperature naturally. The resulting black product was centrifuged and washed with deionized water and absolute alcohol for six times, and finally, the AlOOH-RGO nanocomposites were obtained by drying at 60 °C under vacuum for 24 h. For comparison, the single AlOOH was prepared under the same condition except the addition of the aqueous dispersion GO, and the single RGO was prepared under the same condition except the addition of $Al(NO_3)_3{\cdot}9H_2O$ and urea.

2.3. Preparation of Modified Electrode. Ultrasonic agitation (for 5 min) was used to disperse the AlOOH-RGO nanocomposites into ultrapure water to give a suspension (0.5 mg mL^{-1}). Prior to the surface modification, the bare glassy carbon electrode (GCE) was polished carefully with 1.0, 0.3, and 0.05 μm of alumina powder, respectively, and rinsed with ultrapure water, followed by sonication in alcohol and ultrapure water successively and dried under nitrogen. Then, an aliquot of 5 μL of the suspension was pipetted onto the surface of the electrode, and then, the solvent was evaporated under room temperature to obtain the AlOOH-RGO nanocomposite film modified glass carbon electrode. For comparison, single AlOOH and reduced graphene oxide modified glass carbon electrode were prepared using the same process.

2.4. Electrochemical Behavior of Cd(II) and Pb(II). Square wave anodic stripping voltammetry (SWASV) was used for the observation of electrochemical behavior under optimized conditions. Cd and Pb were deposited at the potential of −1.2 V for 120 s by the reduction of Cd(II) and Pb(II) in 0.1 M NaAc-HAc (pH 6.0). The SPE procedures were performed by stirring the solution with a magnetic stirrer, which is included in the electrodeposition step. The anodic stripping (reoxidation of metal to metal ions) of electrodeposited metal was performed in the potential range of −1.0 to 0.4 V at the following optimized parameters: frequency, 15 Hz; amplitude, 25 mV; increment potential, 4 mV; vs Ag/AgCl. After each measurement, the modified electrode was regenerated in fresh stirred supporting electrolyte by electrolysis at +0.3 V for 140 s to remove the previous residual Cd and Pb from the electrode surface.

2.5. Apparatus. Transmission electron microscopy (TEM) was performed using a JEM-2010 microscope equipped with Oxford INCA EDS operated at 200 kV accelerating voltage (Quantitative method: Cliff Lorimer thin ratio section). Atomic force microscopy (AFM) images were carried out using Nanoscope III (Digital Instruments, Veeco Metrology). X-ray diffraction (XRD) patterns of the samples were obtained with a Philips X'Pert Pro X-ray diffractometer with Cu Kα radiation (1.5418 Å). Fourier transform-infrared (FT-IR) spectroscopy was performed using an IFS 66v/S Vacuum FT-IR. X-ray photoelectron spectroscopy (XPS) analyses of the samples were conducted on a VG ESCALAB MKII spectrometer using an Mg Kα X-ray source (1253.6 eV, 120 W) at a constant analyzer. The energy scale was internally calibrated by referencing the binding energy (Eb) of the C 1s peak at 284.60 eV for contaminated carbon. The Raman measurements were carried out using a DXR Smart Raman spectrometer with 514 nm excitation laser lines (Thermal Fisher).

Electrochemical experiments were recorded using a CHI 660D computer-controlled potentiostat (ChenHua Instruments Co., Shanghai, China) with a standard three-electrode system. A bare glassy carbon electrode (GCE, diameter of 3 mm) or modified GCE served as a working electrode; a platinum wire was used as a counter-electrode with a saturated Ag/AgCl electrode (ChenHua Instruments Co.,Shanghai, China) completing the cell assembly.

3. RESULTS AND DISCUSSION

On the basis of the hydrothermal method, we now designed a green and facile one-pot strategy to obtain well-organized AlOOH-reduced graphite oxide nanocomposites (AlOOH-RGO) directly from graphene oxide (GO) and aluminum nitrate ($Al(NO_3)_3{\cdot}9H_2O$) in the presence of urea, schematically illustrated in Figure 1. First, Al^{3+} ions adsorb onto the surface of GO due to the electrostatic force between the metal ions and negatively charged oxygen-containing functional groups such as carboxyl, hydroxyl, and epoxy groups of GO and the complexation with the oxygen-containing functional groups.[32−34] It is well-known that urea can release CO_2 and OH^- when the temperature of the solution exceeds 80 °C, and

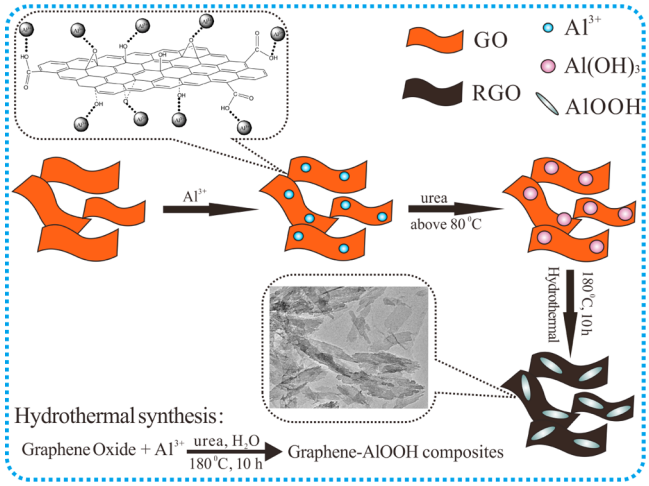

Figure 1. Schematic illustration for the one-pot synthesis of AlOOH-RGO nanocomposites.

then, Al^{3+} ions react with OH^- ions to form $Al(OH)_3$ on the surface of GO nanosheets.[33] AlOOH nanoplates are grown on the surface of graphene nanosheets along with a reduction process of the pristine GO to graphene under a hydrothermal treatment at 180 °C for 10 h. The involved reactions for the formation of AlOOH are suggested as follows:[35]

$$CO(NH_2)_2 + 3H_2O \rightarrow 2NH_4^+ + CO_2 + 2OH^-$$

$$Al^{3+} + 3OH^- \rightarrow Al(OH)_3$$

$$Al(OH)_3 \rightarrow AlOOH + H_2O$$

The AlOOH nanoplates are intercalated into the nanosheets of graphene, which effectively prevents the restacking of the as-reduced graphene nanosheets, and the hybrid AlOOH-RGO nanocomposites are finally obtained. Consequently, the graphene nanosheets keep their high active surface area and the electrochemical performance of AlOOH-RGO nanocomposites compared with AlOOH or RGO is improved, which is proved in the Electrochemical Characterization of AlOOH-Reduced Graphene Oxide Nanocomposites section.

3.1. Morphologic and Structure Characterization of AlOOH-Reduced Graphene Oxide Nanocomposites. Figure 2a shows the XRD patterns of the GO, RGO, AlOOH, and AlOOH-RGO nanocomposites. GO shows a sharp peak centered at $2\theta = 10.6°$, corresponding to the (001) interplanar spacing of 0.83 nm.[36] The characteristic peak of pristine graphite at $2\theta = 26.4°$ disappears after strong oxidation which suggests that graphite is successfully converted to GO after oxidation by Hummer's method.[37,38] After hydrothermal reduction, GO is converted to RGO nanosheets as evidenced by XRD curve. The peak at 10.6° disappears, and a weak and broad diffraction peak (002) appears at 25.4°, a typical pattern of amorphous carbon structure, revealing the stacking of RGO nanosheets is substantially disordered.[37] The interlayer spacing of RGO changes from 0.83 nm for GO to 0.35 nm, which is still a little larger than that of natural graphite (0.34 nm). This can be interpreted by the $\pi-\pi$ stacking interaction between the RGO leading to the formation of the agglomerates.[34] The XRD patterns of the as-synthesized pure AlOOH and hybrid AlOOH-RGO nanocomposites can be indexed to orthorhombic AlOOH (JCPDS no. 01-074-1895). For AlOOH-RGO nanocomposites, no characteristic peak of GO is observed and

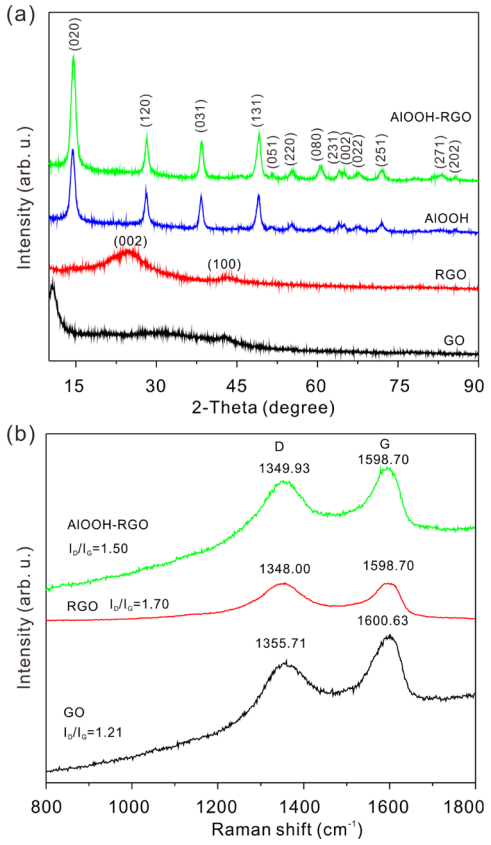

Figure 2. (a) XRD patterns of the GO (black), RGO (red), AlOOH (blue), and AlOOH-RGO nanocomposites (green), respectively. (b) Raman spectra of GO (black), RGO (red), and AlOOH-RGO nanocomposites (green), respectively.

the typical (002) peak of the layered RGO has almost disappeared. This may be ascribed to the fact that GO was reduced to RGO during the hydrothermal reaction and the RGO sheets were exfoliated by decorating AlOOH nanocrystals, leading to the disappearance of the diffraction peaks of RGO (002).[25] The above results suggest that the restacking of the graphene sheets is effectively prevented in the hybrid AlOOH-RGO nanocomposites; thus, the graphene nanosheets keep their high active surface area and conductivity.

Raman spectroscopy is a powerful nondestructive tool to characterize carbonaceous materials for distinguishing ordered and disordered crystal structures of graphene.[34] In general, the Raman spectrum of graphene is characterized by two main features: the G band arising from the first order scattering of the E_{1g} phonon of sp^2 C atoms and the D band arising from a breathing mode of κ-point photons of A_{1g} symmetry.[39,40] The ratio of the D-band intensity (I_D) to the G-band intensity (I_G) represents the disorder level of graphene.[41] The Raman spectra of the GO, RGO, and the hybrid AlOOH-RGO nanocomposites in the range of 800−1800 cm^{-1} are shown in Figure 2b. The G band around 1600 cm^{-1} and the D band around 1355 cm^{-1} are observed in the Raman spectrum of the GO. The I_D/I_G of GO is about 1.2. After hydrothermal reduction, the I_D/I_G of RGO is increased to 1.7. An increased I_D/I_G intensity ratio (1.5) for AlOOH-RGO is also observed, indicating a decrease in the size of the in-plane sp^2 domains, the removal of the oxygen functional groups in the graphene oxide nanosheets, and the reestablishment of the conjugated graphene network (sp^2 carbon).[38,41,42]

dx.doi.org/10.1021/am3010434 | ACS Appl. Mater. Interfaces 2012, 4, 4672−4682

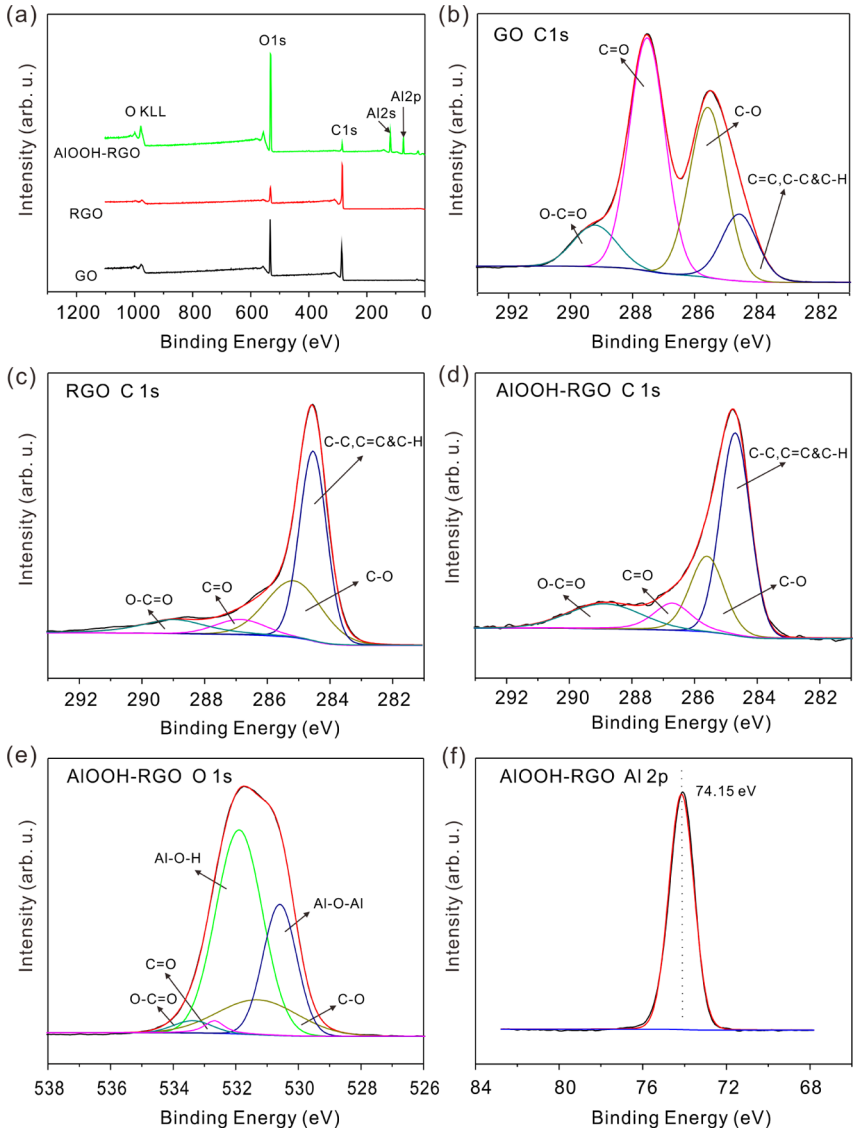

Figure 3. (a) XPS survey spectra of GO (black), RGO (red), and AlOOH-RGO nanocomposites (green), respectively. (b–d) High-resolution C 1s XPS spectra of GO, RGO, and AlOOH-RGO nanocomposites, respectively. (e,f) High-resolution O 1s and Al 2p XPS spectra of AlOOH-RGO nanocomposites, respectively.

The surface composition of GO, RGO, and the AlOOH-RGO nanocomposites is further confirmed by XPS measurements (Figure 3). The binding energies in the XPS measurement are corrected by referencing the C1s peak to 284.5 eV. We can see that, after hydrothermal reduction, RGO showed lower O1s peak than that of GO. Compared to that of GO, the XPS spectrum of the AlOOH-RGO nanocomposites exhibit relatively low C1s peak, and two peaks appear at 118.7 and 74.1 eV corresponding to Al2s and Al2p, which also confirm the presence of AlOOH in the nanocomposites. Figure 3b shows the high-resolution C1s spectrum of GO, which clearly indicates the presence of C−C, C−O, C═O, and COOH groups.[42−44] Upon hydrothermal reduction, the peak intensities for most of the oxygen-containing groups, particularly C═O and C−O, decrease dramatically for RGO (Figure 3c). The high-resolution C1s spectrum of AlOOH-RGO (Figure 3d) shows the similar results to that of RGO due to the reduction of GO to graphene in the hydrothermal synthesis of AlOOH. The removal of most oxygen-containing functional groups implies a good electronic conductivity, which may enable the RGO sheets to serve as the conductive channels between AlOOH nanosheets, and is favorable for stabilizing the electronic and ionic conductivity consequently. The high-resolution O1s spectrum of RGO-AlOOH nanocomposites is shown in Figure 3e. The C−O, C═O, and COOH groups are consistent with the results of high-resolution C1s spectrum, and two new aluminum-containing groups (Al−O−H and Al−O−Al) corresponding to AlOOH appear.[45−47] Figure 3f presents the Al2p high-resolution XPS spectrum of the nanocomposites.[48] In addition, FT-IR spectra analyses can further support the phenomena of the reduction of GO and the formation of AlOOH on the surface of graphene sheets.

FT-IR spectra of GO, RGO, and AlOOH-RGO nanocomposites are shown in Figure 4. Upon oxidation of graphite to GO, the observed peaks of GO confirm the presence of oxygen-containing functional moieties in carbon frameworks, which include the bands at 1065 cm^{-1} (νC−O−C, C−O stretching vibration of epoxide), 1228 cm^{-1} (νC−OH, C−OH stretching vibration), and 1732 cm^{-1} (νC═O, C═O stretching of carbonyl and carboxyl groups located at edges

dx.doi.org/10.1021/am3010434 | ACS Appl. Mater. Interfaces 2012, 4, 4672−4682

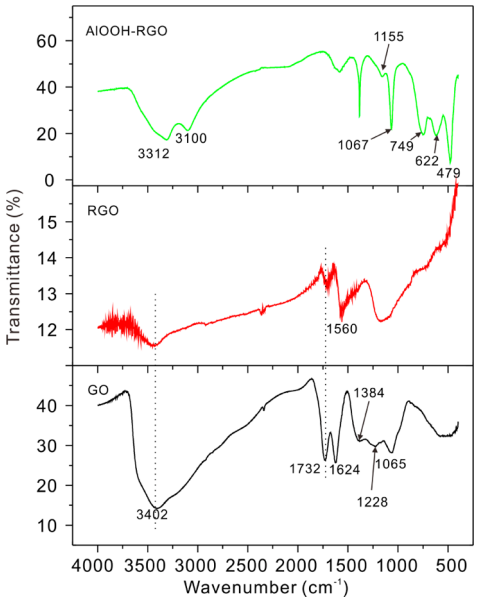

Figure 4. FT-IR spectra of GO (black), RGO (red), and AlOOH-RGO nanocomposites (green), respectively.

of the GO networks).[49] In addition, we observe the O−H deformation peak at 1384 cm^{-1} and a strong and broad absorption at 3402 cm^{-1} due to O−H stretching vibration.[49,50] The spectrum also depicts a peak at 1624 cm^{-1} which corresponds to the remaining sp^2 character.[49] After hydrothermal reduction, the peak intensities of oxygen-containing functional groups in RGO decrease, which is consistent with the Raman and XPS results, and a new adsorption band corresponding to the aromatic skeletal C=C stretching vibration of the graphene sheets appears at 1560 cm^{-1}.[37,50] While in the FT-IR spectrum of AlOOH-RGO nanocomposites, the absorption peaks related to the oxygen-containing groups vanish. In addition, some absorption bands of AlOOH appear. In detail, the bands at 3312 and 3100 cm^{-1} belong to the ν_{as}(Al)O−H and ν_{s}(Al)O−H stretching vibrations, respectively.[51,52] The band at 1067 cm^{-1} and the shoulder at 1155 cm^{-1} are assigned to the δs Al−O−H and δas Al−O−H modes of AlOOH, respectively, and the three bands at 749, 622, and 479 cm^{-1} represent the vibration mode of AlO_6.[53,54] Consequently, FT-IR analysis also confirms that the AlOOH-RGO nanocomposites were obtained.

Figure 5a shows a typical AFM image of an exfoliated GO dispersion in water after deposition on a freshly cleaved mica surface. The average thickness of as-prepared GO measured from the height profile of the AFM image is about 0.895 nm, which corresponds to a single-layer GO.[55] The larger thickness of GO than the theoretical values of 0.78 nm for single-layer graphene may arise from oxygen-containing groups on the surfaces.[34,55,56] It should be highly promising for this ideal single-atom-thick graphene nanosheet as a support to anchor functional nanomaterials to form new nanocomposites. The AFM image of the composite of AlOOH-RGO is shown in Figure S1, Supporting Information, which is in consist with the TEM image. The average thickness of RGO in the AlOOH-RGO composite measured from the height profile is about 0.6

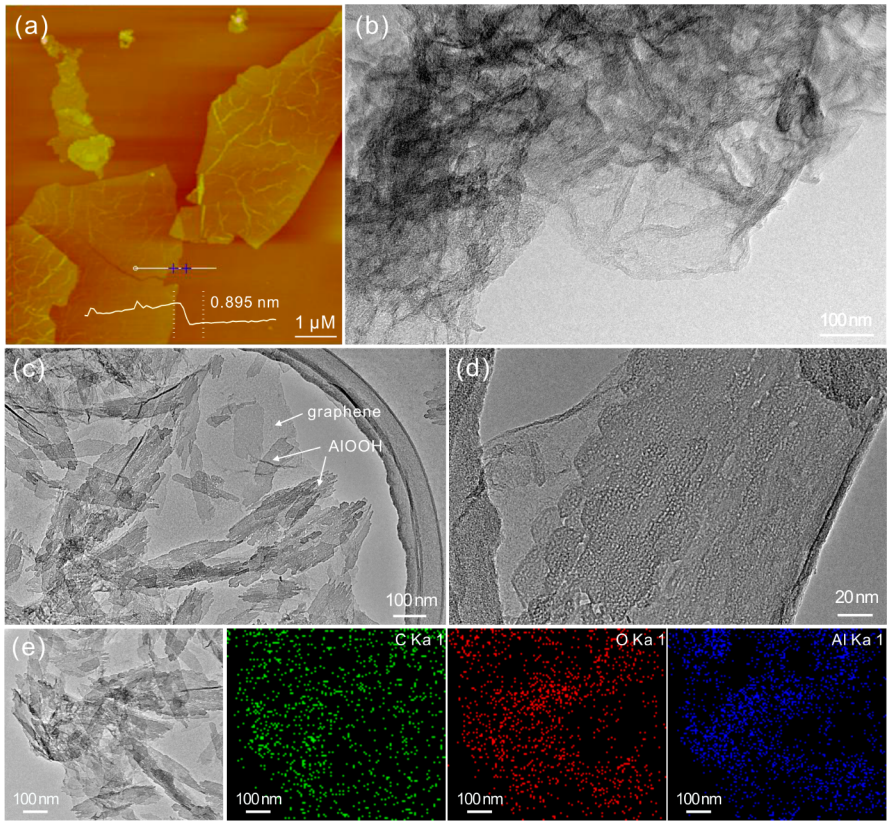

Figure 5. (a) A tapping mode AFM image of GO with height profile. (b) TEM image of RGO. (c and d) TEM images at different magnification of the AlOOH-RGO nanocomposites. (e) TEM image of the AlOOH-RGO nanocomposites and the corresponding elemental mapping images of C, O, and Al.

nm, and the measured thickness of AlOOH in the AlOOH-RGO composite is from 7 to 20 nm.

The TEM image of as-reduced RGO nanosheets (Figure 5b) shows that the RGO has corrugations and scrollings due to the agglomerate of the graphene sheet. Figure 5c,d gives the TEM and high-resolution TEM images of AlOOH-RGO nanocomposites. We can see that thin AlOOH nanoplates decorate on both sides of graphene nanosheets and exhibit loose lamellar structures. Except that it seems thinner, the AlOOH nanoplates in composites are not very different from those synthesized without the addition of GO (Figure S2, Supporting Information). As AlOOH nanoplates are distributed on the surface of graphene nanosheets, the restacking of graphene nanosheets is effectively prevented, thus avoiding the loss of their highly active surface area. The TEM images of the AlOOH-RGO nanocomposites and the corresponding elemental mapping show homogeneous distribution of AlOOH in the entire range (Figure 5e). This kind of configuration make these nanocomposites have better electrochemical performance than both AlOOH and RGO only, which will be shown in the next parts.

3.2. Electrochemical Characterization of AlOOH-Reduced Graphene Oxide Nanocomposites. The cyclic voltammetric response of bare, AlOOH nanoplates, and AlOOH-RGO nanocomposite modified GCE has been examined using the $Fe(CN)_6^{3-/4-}$ redox couple in neutral solution of 5 mM $Fe(CN)_6^{3-/4-}$ containing 0.1 M KCl (Figure 6a). As compared with the bare GCE, the anodic and cathodic peaks decreased at the AlOOH modified electrode. This result indicates that the rate of electron transfer at the electrode surface is hindered with the attachment of AlOOH to GCE surface, which proves that AlOOH do not give a good conductivity. After modification with the AlOOH-RGO nanocomposites, the electrode shows the highest current. This reveals that the introduction of RGO may provide the necessary conduction pathways on the electrode surface due to its large 2-D electrical conductivity,[22] and the combination of AlOOH and RGO may provide a better electrochemical catalytic behavior, thus resulting in the promotion of the electron transfer process at the modified electrode surface.

Electrochemical impedance spectrum (EIS) was employed to further characterize the interface properties of the modified electrodes. In a typical Nyquist plot, the semicircle portion correspond to the electron-transfer resistance (R_{et}) at higher frequency range while a linear part at lower frequency range represents the diffusion limited process. As seen in Figure 6b, the R_{et} value corresponding to the bare GCE is about 200 Ω. After modification with AlOOH, the semicircle domain with R_{et} value increased to about 700 Ω, which is ascribed to that the poor conductivity of AlOOH creates a further barrier for electron transfer at the modified electrode surface. However, for AlOOH-RGO nanocomposite modified GCE, compared with AlOOH, the semicircle domain with R_{et} value distinctly decreased and displayed an almost straight line, suggesting the promotion of electron transfer process at the modified electrode surface. These results were supported by the above cyclic voltammogram data.

Figure 6c presents the SWASV analytical characteristics of bare, AlOOH, RGO, and AlOOH-RGO modified GCE. When the accumulation process was carried out for 120 s at −1.2 V in a solution containing 1.0 μM each of Cd(II) and Pb(II) in 0.1 M acetate buffer (pH 5.0) without deaeration, nearly no peaks were observed at bare (black curve) GCE in the potential range

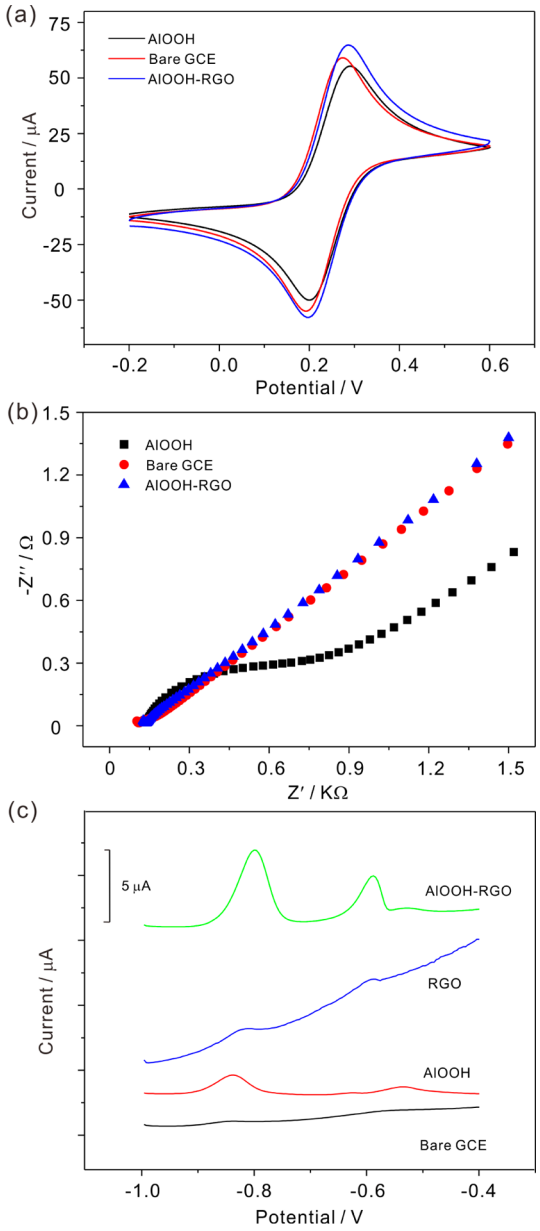

Figure 6. Cyclic voltammograms (a) and Nyquist diagram of electrochemical impedance spectra (b) for bare, AlOOH, and AlOOH-RGO nanocomposite modified GCE in the solution of 5 mM $Fe(CN)_6^{3-/4-}$ containing 0.1 M KCl. (c) SWASVs for 1.0 μM each of Cd(II) and Pb(II) on bare (black curve), AlOOH (red curve), RGO (blue curve), and AlOOH-RGO nanocomposite (green curve) modified GCE in 0.1 M acetate buffer solution (pH 6.0). Deposition potential, −1.2 V; deposition time, 120 s; amplitude, 25 mV; increment potential, 4 mV; frequency, 15 Hz; vs Ag/AgCl.

of −1.0 to +0.4 V. For AlOOH nanoplates (red curve) and RGO (blue curve) modified GCE, there are only very weak peaks. This is probably due to that RGO has a good conductivity but a relative poor absorbability toward the target heavy metal ions, and AlOOH has a good absorbability toward the target heavy metal ions but a poor conductivity. However, the much higher and sharper peak current for the two target metal ions was obtained at the AlOOH-RGO nanocomposite modified electrode (green curve). (Individually, Cd(II) and Pb(II) can be identified at potentials of −0.8 and −0.6 V, respectively.) The active electrode surface of AlOOH-RGO and

dx.doi.org/10.1021/am3010434 | ACS Appl. Mater. Interfaces 2012, 4, 4672−4682

RGO are calculated to be 5.77×10^{-2} and 6.28×10^{-2} cm^{-2} according to the Randles-Sevcik equation: $i_p = (2.69 \times 10^5) n^{3/2} ACD^{1/2} v^{1/2}$ (Figure S3, Supporting Information). The calculated active electrode surface of AlOOH-RGO and RGO are almost the same. However, the response current for AlOOH-RGO is obviously larger than that for GO. This result demonstrates that the increase in stripping currents after introduction of nonconducting AlOOH is mainly attributed to the good absorbability of AlOOH, which help to accumulate Cd(II) and Pb(II) on the electrode surface. It should be noted that, although strong peaks for Cd(II) and Pb(II) were obtained at GO modified electrode due to lots of functional groups acting as anchor sites to adsorb heavy metal ions on GO surface, we found that it was very hard to desorb the target metal ions (Figure S4, Supporting Information), so pure GO modified electrode cannot be reused conveniently and is not suited for monitoring the heavy metal ions; thus, its implication in practice is limited.

3.3. Optimization of Experimental Conditions. In order to get the maximum sensitivity for trace heavy metal ion detection with AlOOH-RGO modified GCE, the voltammetric parameters (pH value, deposition potential, and deposition time) were optimized in solution containing 0.5 μM each of Cd(II) and Pb(II). The effect of different supporting electrolytes on SWASV response (Figure S5, Supporting Information) and the effect of the amounts of the AlOOH-RGO on SWASV response (Figure S6, Supporting Information) were also studied to optimize the experimental conditions.

The pH value may have an effect on the voltammetric response; thus, it is essential to select a proper pH value. The effect of pH on the voltammetric response was investigated in the pH range from 4.0 to 7.0 in 0.1 M acetate buffer solution. As shown in Figure 7a, the peak current for both Cd(II) and Pb(II) increased as the pH was changed from 4.0 to 6.0, reaching a maximum at pH 6.0, and then decreased up to pH 7.0. As mentioned above, in stripping analysis, the efficient preconcentration of the target analyte onto a certain substrate is significant. Thus, the voltammetric signal, such as Pb(II), was controlled by how well the electrode materials can capture Pb(II), which are subsequently accumulated on the electrode surface. For this reason, we suggested that this is consistent with our results reported previously that the adsorption capacity of the AlOOH for Pb(II) is strong in near-neutral conditions and poor in strongly acidic conditions.[14] The decrease of the stripping signal at higher pH 7.0 may be related with the hydrolysis of metal ions. Thus, pH 6.0 in 0.1 M acetate buffer solution was selected for stripping measurements.

In stripping analysis, the application of adequate deposition potential is very important to achieve the best sensitivity. Thus, the effect of the deposition potential on the peak current after 120 s accumulation was studied in the potential range from −0.9 to −1.3 V in 0.1 M acetate buffer solution at pH 6.0. The obtained results are shown in Figure 7b. When the deposition potential shifts from −0.9 to −1.2 V, the stripping peak currents for Cd(II) and Pb(II) increased, and the peak currents reached a maximum at potential −1.2 V. When a deposition potential more negative than −1.2 V was employed, a decrease on the response was observed for both Cd(II) and Pb(II), which is probably due to the competitive generation of H_2. Thus, we choose −1.2 V as the optimal deposition potential for the subsequent experiment.

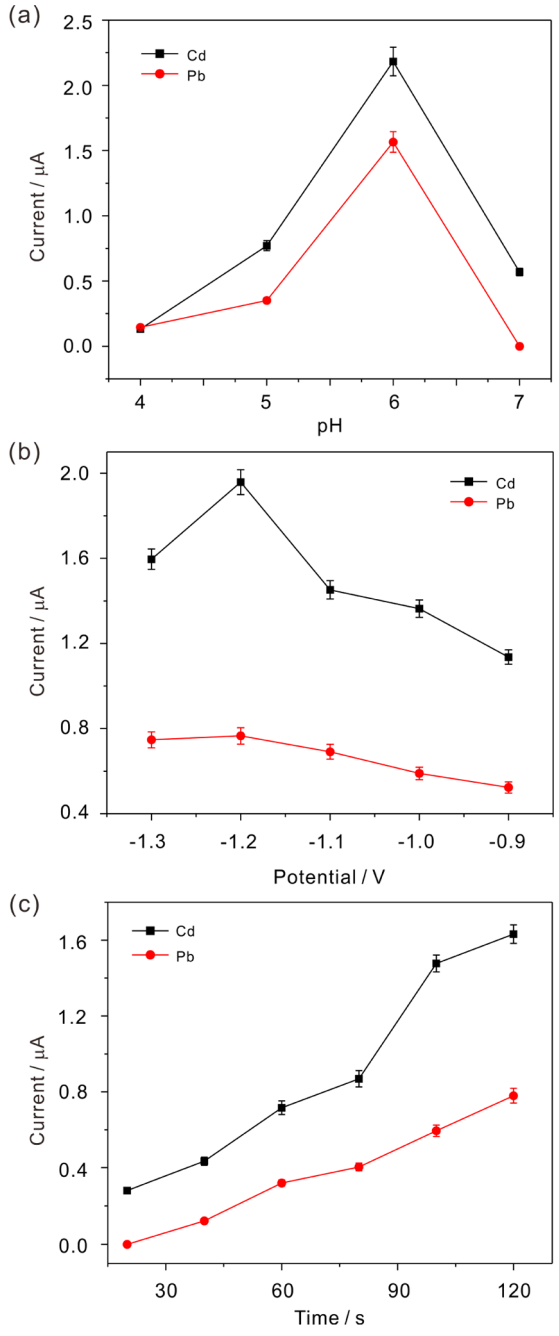

Figure 7. Optimum experimental conditions. Influence of (a) pH value; (b) deposition potential; and (c) deposition time on the voltammetric response of AlOOH-RGO nanocomposite modified GCE. Data were evaluated by SWASV of 0.5 μM Cd(II) and Pb(II). SWASV conditions are identical to Figure 6c.

As the deposition time may affect the detection limit and the sensitivity, different deposition times were studied in this work. The dependence of peak currents on the deposition time for two target metal ions was depicted in Figure 7c. The response of the stripping peak currents of Cd(II) and Pb(II) enhanced with the increase of the deposition time varying from 20 up to 120 s is due to the increased amount of analytes on the modified electrode surface. Although increasing the deposition time improves the sensitivity, it also lowers the upper detection limit due to the surface saturation at high metal ion concentrations.[57] Therefore, to achieve lower detection limit

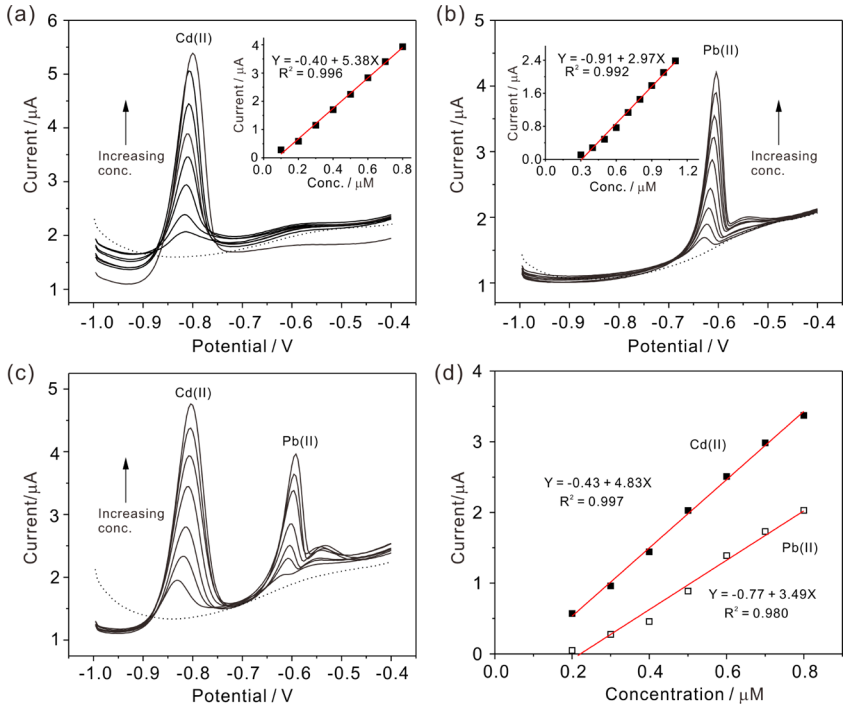

Figure 8. SWASV response of the AlOOH-RGO nanocomposite modified GCE for the individual analysis of (a) Cd(II) over a concentration range of 0.1 to 0.8 μM and (b) Pb(II) over a concentration range of 0.3 to 1.1 μM. Inset in panel a and b is corresponding linear calibration plot of peak current against Cd(II) and Pb(II) concentrations, respectively. (c) SWASV response of the AlOOH-RGO nanocomposite modified GCE for the simultaneous analysis of Cd(II) and Pb(II) over a concentration range of 0.2 to 0.8 μM. (d) The respective calibration curves of Cd(II) and Pb(II) corresponding to panel c. Each addition increased the concentration by 0.1 μM. Supporting electrolyte, 0.1 M acetate buffer solution (pH 6.0); SWASV conditions are identical to Figure 6c. The dotted line refers to the baseline.

Table 1. Comparison of Individual and Simultaneous Analysis

	analyte	linear range, μM	limit of detection (LOD), M	correlation coefficient	sensitivity (μA μM^{-1})
individual analysis	Cd(II)	0.1−0.8	4.46×10^{-11}	0.996	5.38
	Pb(II)	0.3−1.1	7.60×10^{-11}	0.992	2.97
simultaneous analysis	Cd(II)	0.2−0.8	3.52×10^{-11}	0.997	4.83
	Pb(II)	0.2−0.8	9.32×10^{-11}	0.980	3.49

and wider response range and take the efficiency into account, 120 s was chosen as the deposition time.

3.4. Stripping Behavior toward Cd(II) and Pb(II). Under the optimal experimental conditions, Cd(II) and Pb(II) were determined individually and simultaneously at the AlOOH-RGO electrode using SWASV. Figure 8a shows the SWASV response for Cd(II) at various concentrations, and the corresponding calibration curve was derived accordingly (inset in Figure 8a). Cd(II) is detected at potentials of approximately −0.8 V with well-defined peaks, and the stripping peak current is proportional to the concentration of Cd(II) from 0.1 to 0.8 μM. The linearization equations were $i/\mu A = -0.40 + 5.38c/\mu M$, with the correlation coefficients of 0.996. The limit of detection (LOD) was calculated to be 4.46×10^{-11} M (3σ method). The SWASV responses of the AlOOH-RGO electrode toward Pb(II) over a concentration range of 0.3 to 1.1 μM was shown in Figure 8b. Pb(II) is detected at potentials of approximately −0.6 V with well-defined peaks. The linearization equation was $i/\mu A = -0.91 + 2.97c/\mu M$, with the correlation coefficient of 0.992 (inset of Figure 8b) and with the LOD of 7.60×10^{-11} M (3σ method).

When analyzing Cd(II) and Pb(II) simultaneously, as shown in Figure 8c, well-defined peaks were observed for both two target metal ions. As seen, the modified electrode shows individual peaks at approximately −0.8 and −0.6 V for Cd(II) and Pb(II), respectively, in their coexistence. The separation between the voltammetric peaks is large enough, and hence, the simultaneous or the selective detection using the AlOOH-RGO nanocomposite modified electrode is feasible. As shown in Figure 8d, the corresponding calibration curves for Cd(II) and Pb(II) were built from 0.2 μM up to 0.8 μM. The linearization equations were $i/\mu A = -0.43 + 4.83c/\mu M$ and $i/\mu A = -0.77 + 3.49c/\mu M$ for Cd(II) and Pb(II), respectively, with the corresponding correlation coefficients of 0.997 and 0.980, respectively. The LODs were calculated to be 3.52×10^{-11} M for Cd(II) and 9.32×10^{-11} M for Pb(II) (Table 1), which is significantly lower compared with other carbon nanomaterials in electrochemical detection of heavy metal ions (Table S1, Supporting Information). These obtained LODs are very well below the guideline value given by the World Health Organization (WHO).

In particular, it should be noted that, although the sensing properties of LOD and sensitivity at the AlOOH-RGO nanocomposites were not the best compared with some work reported previously, the obtained sensing performance could be further improved by optimizing the synthesis conditions, such as reactant ratio, reaction temperature, reaction time, etc. Most

importantly, this material showed a great potential for implication in practice in the sections below.

3.5. Evaluation of Selectivity, Interferences, Stability, and Repeatability. Some other common heavy metal ions were tested to evaluate the selectivity of AlOOH-RGO nanocomposite modified electrode. It was found that Zn(II), Cu(II), and Hg(II) could also be detected at about −1.12, −0.05, and 0.25 V, respectively (Figure S7, Supporting Information). The obtained responses were not significantly weaker than that of Cd(II) and Pb(II). This indicated that AlOOH-RGO nanocomposite modified electrode did not have a good selectivity, which is due to that AlOOH has significant affinities to some heavy metal ions. However, as different heavy metal ions are stripped with the appearance of each stripping peak at different position and the stripping peak of Zn(II), Cu(II), and Hg(II) are far away from that of Cd(II) and Pb(II), there is no conflict with the simultaneous detection of Cd(II) and Pb(II). Furthermore, this implies that the proposed electrode could be used for simultaneous detection of several heavy metals including Zn(II), Cu(II), and Hg(II).

Mutual interference is a common problem existing in detection of several metal ions simultaneously. Thus, we next seek to study the mutual interferences between Cd(II) and Pb(II) at the AlOOH-RGO nanocomposite modified electrode. When fixing the concentration of Pb(II) but increasing the concentration of Cd(II), as shown in Figure 9a, the peak current of Cd(II) linearly increased while the peak current of Pb(II) almost remains the same. Similarly, when fixing the concentration of Cd(II) but increasing the concentration of Pb(II), as shown in Figure 9b, the peak current of Pb(II) linearly increased while the peak current of Cd(II) almost remains the same. All the results indicate that, at low concentrations, there is no obvious mutual interferences between Cd(II) and Pb(II) at the AlOOH-RGO nanocomposite modified electrode when detecting the two target metal ions simultaneously.

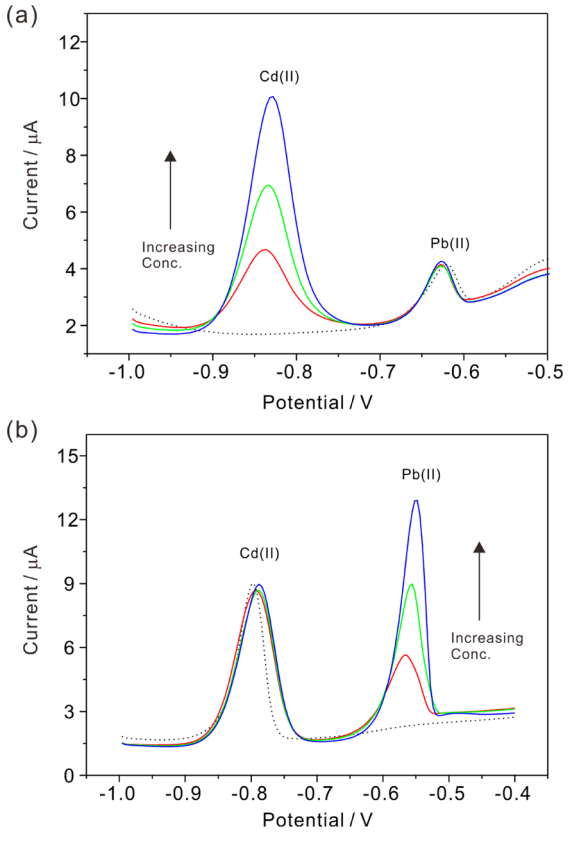

Figure 9. SWASV response of the AlOOH-RGO nanocomposite modified GCE: (a) at 0, 1.0, 1.5, and 2.0 μM Cd(II) in the presence of 1.0 μM Pb(II) in 0.1 M NaAc-HAc solution (pH 6.0); (b) at 0, 1.0, 1.5, and 2.0 μM Pb(II) in the presence of 1.0 μM Cd(II) in 0.1 M NaAc-HAc solution (pH 6.0). SWASV conditions are identical to Figure 6c. Dotted line in panels a and b represents the SWASV response in the absence of Cd(II) and Pb(II), respectively.

On the other hand, the interference study was considered by adding various foreign substances into a standard solution containing 1.5 μM each of Cd(II) and Pb(II) under the above-optimized conditions. When the change of peak current exceeds 5.0% relative error, it is considered that this substance causes obvious interference. It was found that many common anions such as PO_4^{3-}, SO_4^{2-}, NO_3^- and Cl^-, which exceeded 50-fold concentration, had no significant influences on the stripping peak current of Cd(II) and Pb(II). A 50-fold concentration of various common cations, such as K^+, Na^+, Mg^{2+}, Ca^{2+}, and Al^{3+} also had no interferences with Cd(II) and Pb(II) detection, because they were normally inactive by voltammetry. As for Zn^{2+}, it did not have any significant influences until the concentration of Zn^{2+} was increased to 20-fold (Figure S8, Supporting Information). This might be due to the fact that many available deposition and/or adsorption sites could be occupied by Zn^{2+} at high concentrations. A 5-fold concentration of Cu^{2+} was found to heavily suppress the peak current of Cd(II) (decreased by about 85%) and Pb(II) (decreased by about 63%). This phenomenon has been reported by many in the literature, which is probably related to the formation of the Cu−Cd and Cu−Pb intermetallic compounds.[58−61] Even equal concentration of Hg^{2+} was found to obviously increase the stripping signals of Cd(II) (increased by about 67%) and Pb(II) (increased by about 31%), which is due to the formation of mercury film at the modified electrode surface. Consequently, it causes Cd(II) and Pb(II) to be reduced more easily and increases the stripping peak current due to the formation of amalgam.[3]

As a common macromolecular organic material in nature water, humic acid (HA) was also considered to evaluate the interference with the anodic peak currents of 1.0 μM Cd(II) and 1.0 μM Pb(II) (Figure S9, Supporting Information). It was found that 5 ppm of HA began to have obvious influences on the stripping peak current of Cd(II) (decreased by about 11%) and Pb(II) (decreased by about 43%). Thirty ppm of HA heavily suppressed the peak current of Cd(II) (decreased by about 56%) and Pb(II) (decreased by about 87%). These results were consistent with that HA has high complex capacity with heavy metal ions and was applied to remove heavy metal ions from water.[62] However, the approach of eliminated interference will not be required for trace levels of the heavy metal ions in unpolluted drinking water samples.

To evaluate the stability of the AlOOH-RGO nanocomposite modified electrode, a series of 15 time repetitive measurements of SWASV response for 1.0 μM Cd(II) in 0.1 M NaAc-HAc solution (pH 6.0) was performed. As shown in Figure 10, the stripping current of the electrode is highly reproducible with a relative standard deviation of 2.21%. Therefore, the AlOOH-RGO nanocomposite modified electrode has an excellent stability for repetitive stripping measurements in the experimental conditions. The repeatability between different electrodes was estimated by comparing the stripping peak current of

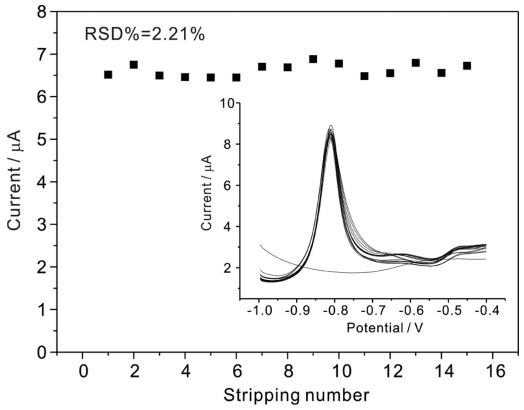

Figure 10. The stability of 15 times repetitive measurements of SWASV response for 1.0 μM Cd(II) on the AlOOH-RGO nanocomposite modified GCE in 0.1 M NaAc-HAc solution (pH 6.0). SWASV conditions are identical to Figure 6c.

0.5 μM Cd(II) and Pb(II) at different electrodes (n = 6). The RSDs were 2.7% for Cd(II) and 3.1% for Pb(II), revealing that the repeatability between different electrodes is good. In addition, we also found that the AlOOH-RGO nanocomposite modified electrode can be used for a long total experimental time without regenerating the surface time after time.

3.6. Real Sample Analysis. For the purpose of practical application of the present electrode, a test on a real water sample has been performed. The real sample was collected from Dongpu Reservoir in Hefei City, Anhui province, China. The real sample was diluted with 0.1 M NaAc-HAc buffer solution (pH 6.0) in a ratio of 1:1, and no further sample treatment was done. Standard additions of Cd(II) were performed in the diluted sample. The SWASV response and the corresponding calibration plots are shown in Figure S10a, Supporting Information. With the standard additions of Cd(II), linear plots were obtained and used for the calculation of Cd(II) concentration in the real sample. The concentration of Cd(II) in the real sample was calculated to be 2.7 nM. Similarly, the standard-additions method was adopted to determine the concentration of Pb(II) in the real sample. The concentration of Pb(II) in the real sample was calculated to be 3.2 nM based on the corresponding calibration plots (Figure S10b, Supporting Information).

In order to evaluate the validity of the proposed method for the determination, recovery studies are carried out on real samples to which known amount of target metal ion is added. As shown in Table 2, the recovery obtained is varied from 96.3% to 102.2%. These results reveal that the proposed AlOOH-RGO nanocomposites have important practical application potential.

4. CONCLUSIONS

In the present study, for the first time, AlOOH-RGO nanocomposites with excellent electrochemical properties have been successfully and directly synthesized from GO through a green, facile, effective, and scalable hydrothermal method. The AlOOH nanoplates were homogeneously attached on the graphene sheets and effectively prevented the graphene sheets from aggregating together. In combination of the advantages of both AlOOH and graphene sheets, the AlOOH-RGO nanocomposites are a promising material which possesses good sensitivity, high stability, excellent practical applicability, and long-term usage possibility in electrochemical detecting heavy metal ions. More significantly, as a new material, the AlOOH-RGO nanocomposites may possess many unknown properties waiting to be explored.

Table 2. Determination of Cd(II) and Pb(II) in Real Sample (n = 5)

	original (nM)	added (μM)	found (μM)	recovery (%)	RSD (%)
Cd(II)	2.7	0.05	0.0538	102.2	3.81
Pb(II)	3.2	0.1	0.0995	96.3	4.72

■ ASSOCIATED CONTENT

Ⓢ Supporting Information

Comparison of performance for electrochemical determination of Cd(II) and Pb(II) with various carbon nanomaterials, AFM image of AlOOH-RGO, TEM image of AlOOH nanoplates, scan rate study at RGO and AlOOH-RGO modified GCE, SWASV response on GO modified GCE, SWASV response in different supporting electrolytes on AlOOH-RGO modified GCE, the effect of the amount of AlOOH-RGO on SWASV response, SWASV response of the AlOOH-RGO nanocomposite modified GCE for the individual analysis of Zn(II), Cu(II), and Hg(II), the interference of the concentrations of Zn(II) and humic acid on the anodic peak currents of Cd(II) and Pb(II), and SWASV response of real sample analysis. This information is available free of charge via the Internet at http://pubs.acs.org/.

■ AUTHOR INFORMATION

Corresponding Author

*E-mail: xingjiuhuang@iim.ac.cn. Tel.: +86-551-5591142. Fax: +86-551-5592420.

Author Contributions

§These two authors contributed equally to this work.

Notes

The authors declare no competing financial interest.

■ ACKNOWLEDGMENTS

This work was supported by the One Hundred Person Project of the Chinese Academy of Sciences, China, the National Key Scientific Program-Nanoscience and Nanotechnology (No. 2011CB933700), National Natural Science Foundation of China (Grant No. 21103198), and the China Postdoctoral Science Foundation (Nos. 20110490386 and 2011M501073).

■ REFERENCES

(1) Gong, J. M.; Zhou, T.; Song, D. D.; Zhang, L. Z.; Hu, X. L. *Anal. Chem.* **2010**, *82*, 567.
(2) Ferreira, M. A.; Barros, A. A. *Anal. Chim. Acta* **2002**, *459*, 151.
(3) Wu, H. P. *Anal. Chem.* **1996**, *68*, 1639.
(4) Vassileva, E.; Proinova, I.; Hadjiivanov, K. *Analyst* **1996**, *121*607.
(5) Wang, J.; Ashley, K.; Marlow, D.; England, E. C.; Carlton, G. *Anal. Chem.* **1999**, *71*, 1027.
(6) Liu, Y.; Liang, P.; Guo, L. *Talanta* **2005**, *68*, 25.
(7) Liu, R.; Liang, P. *J. Hazard. Mater.* **2008**, *152*, 166.
(8) Faraji, M.; Yamini, Y.; Saleh, A.; Rezaee, M.; Ghambarian, M.; Hassani, R. *Anal. Chim. Acta* **2010**, *659*, 172.
(9) Shi, L.; Liu, X.; Li, H.; Niu, W.; Xu, G. *Anal. Chem.* **2006**, *78*, 1345.
(10) Du, D.; Wang, M.; Zhang, J.; Cai, J.; Tu, H.; Zhang, A. *Electrochem. Commun.* **2008**, *10*, 85.

(11) Du, D.; Ye, X.; Zhang, J.; Zeng, Y.; Tu, H.; Zhang, A.; Liu, D. *Electrochem. Commun.* **2008**, *10*, 686.
(12) Gong, J.; Wang, L.; Miao, X.; Zhang, L. *Electrochem. Commun.* **2010**, *12*, 1658.
(13) Liu, G. H.; Zhu, Y. F.; Zhang, X. R.; Xu, B. Q. *Anal. Chem.* **2002**, *74*, 6279.
(14) Zhang, Y.-X.; Yu, X.-Y.; Jin, Z.; Jia, Y.; Xu, W.-H.; Luo, T.; Zhu, B.-J.; Liu, J.-H.; Huang, X.-J. *J. Mater. Chem.* **2011**, *21*, 16550.
(15) Zhang, Y.-X.; Jia, Y.; Jin, Z.; Yu, X.-Y.; Xu, W.-H.; Luo, T.; Zhu, B.-J.; Liu, J.-H.; Huang, X.-J. *CrystEngComm* **2012**, *14*, 3005.
(16) Granados-Correa, F.; Corral-Capulin, N.; Olguín, M.; Acosta-León, C. *Chem. Eng. J.* **2011**, *171*, 1027.
(17) Wu, K.; Hu, S.; Fei, J.; Bai, W. *Anal. Chim. Acta* **2003**, *489*, 215.
(18) Sun, D.; Xie, X.; Cai, Y.; Zhang, H.; Wu, K. *Anal. Chim. Acta* **2007**, *581*, 27.
(19) Zhu, L. D.; Tian, C. Y.; Yang, R. L.; Zhai, J. L. *Electroanalysis* **2008**, *20*, 527.
(20) Li, D. Y.; Jia, J. B.; Wang, J. G. *Talanta* **2010**, *83*, 332.
(21) Aragay, G.; Pons, J.; Merkoci, A. *J. Mater. Chem.* **2011**, *21*, 4326.
(22) Pumera, M.; Ambrosi, A.; Bonanni, A.; Chng, E. L. K.; Poh, H. L. *TrAC, Trends Anal. Chem.* **2010**, *29*, 954.
(23) Brownson, D. A. C.; Banks, C. E. *Analyst* **2010**, *135*, 2768.
(24) Williams, G.; Seger, B.; Kamat, P. V. *ACS Nano* **2008**, *2*, 1487.
(25) Xu, C.; Wang, X.; Zhu, J. *J. Phys. Chem. C* **2008**, *112*, 19841.
(26) Liu, J.; Fu, S.; Yuan, B.; Li, Y.; Deng, Z. *J. Am. Chem. Soc.* **2010**, *132*, 7279.
(27) Si, Y.; Samulski, E. T. *Chem. Mater.* **2008**, *20*, 6792.
(28) Gong, J. M.; Zhou, T.; Song, D. D.; Zhang, L. Z. *Sens. Actuators, B: Chem.* **2010**, *150*, 491.
(29) Li, J.; Guo, S. J.; Zhai, Y. M.; Wang, E. K. *Anal. Chim. Acta* **2009**, *649*, 196.
(30) Li, J.; Guo, S. J.; Zhai, Y. M.; Wang, E. K. *Electrochem. Commun.* **2009**, *11*, 1085.
(31) Hummers, W. S.; Offeman, R. E. *J. Am. Chem. Soc.* **1958**, *80*, 1339.
(32) Chen, S.; Zhu, J.; Wu, X.; Han, Q.; Wang, X. *ACS Nano* **2010**, *4*, 2822.
(33) Zhu, X.; Zhu, Y.; Murali, S.; Stoller, M. D.; Ruoff, R. S. *ACS Nano* **2011**, *5*, 3333.
(34) Gao, Z.; Wang, J.; Li, Z.; Yang, W.; Wang, B.; Hou, M.; He, Y.; Liu, Q.; Mann, T.; Yang, P.; Zhang, M.; Liu, L. *Chem. Mater.* **2011**, *23*, 3509.
(35) Chen, X. Y.; Huh, H. S.; Lee, S. W. *Nanotechnology* **2007**, *18*, 285608.
(36) Xu, C.; Wu, X. D.; Zhu, J. W.; Wang, X. *Carbon* **2008**, *46*, 386.
(37) Su, J.; Cao, M.; Ren, L.; Hu, C. *J. Phys. Chem. C* **2011**, *115*, 14469.
(38) Wang, G.; Yang, J.; Park, J.; Gou, X.; Wang, B.; Liu, H.; Yao, J. *J. Phys. Chem. C* **2008**, *112*, 8192.
(39) Tuinstra, F.; Koenig, J. L. *J. Chem. Phys.* **1970**, *53*, 1126.
(40) Ferrari, A. C.; Robertson, J. *Phys. Rev. B* **2000**, *61*, 14095.
(41) Li, H.; Zhu, G.; Liu, Z.-H.; Yang, Z.; Wang, Z. *Carbon* **2010**, *48*, 4391.
(42) Stankovich, S.; Dikin, D. A.; Piner, R. D.; Kohlhaas, K. A.; Kleinhammes, A.; Jia, Y.; Wu, Y.; Nguyen, S. T.; Ruoff, R. S. *Carbon* **2007**, *45*, 1558.
(43) Al-Mashat, L.; Shin, K.; Kalantar-zadeh, K.; Plessis, J. D.; Han, S. H.; Kojima, R. W.; Kaner, R. B.; Li, D.; Gou, X.; Ippolito, S. J.; Wlodarski, W. *J. Phys. Chem. C* **2010**, *114*, 16168.
(44) Song, H. J.; Zhang, L. C.; He, C. L.; Qu, Y.; Tian, Y. F.; Lv, Y. *J. Mater. Chem.* **2011**, *21*, 5972.
(45) Sahoo, N. G.; Cheng, H. K. F.; Li, L.; Chan, S. H.; Judeh, Z.; Zhao, J. *Adv. Funct. Mater.* **2009**, *19*, 3962.
(46) Kloprogge, J. T.; Duong, L. V.; Wood, B. J.; Frost, R. L. *J. Colloid Interface Sci.* **2006**, *296*, 572.
(47) Zhang, X.; Wu, Y.; Liu, G.; He, S.; Yang, D. *Thin Solid Films* **2008**, *516*, 5020.
(48) Shen, S. C.; Chen, Q.; Chow, P. S.; Tan, G. H.; Zeng, X. T.; Wang, Z.; Tan, R. B. H. *J. Phys. Chem. C* **2006**, *111*, 700.
(49) Li, Y.; Lv, X.; Lu, J.; Li, J. *J. Phys. Chem. C* **2010**, *114*, 21770.
(50) Nethravathi, C.; Rajamathi, M. *Carbon* **2008**, *46*, 1994.
(51) Fripiat, J. J.; Bosmans, H. J.; Rouxhet, P. G. *J. Phys. Chem.* **1967**, *71*, 1097.
(52) Wickersheim, K.; Korpi, G. *J. Chem. Phys.* **1965**, *42*, 579.
(53) Zhang, J.; Wei, S.; Lin, J.; Luo, J.; Liu, S.; Song, H.; Elawad, E.; Ding, X.; Gao, J.; Qi, S.; Tang, C. *J. Phys. Chem. B* **2006**, *110*, 21680.
(54) Kiss, A. B.; Keresztury, G.; Farkas, L. *Spectrochim. Acta, Part A: Mol. Spectrosc.* **1980**, *36*, 653.
(55) Gómez-Navarro, C.; Weitz, R. T.; Bittner, A. M.; Scolari, M.; Mews, A.; Burghard, M.; Kern, K. *Nano Lett.* **2007**, *7*, 3499.
(56) Stankovich, S.; Piner, R. D.; Nguyen, S. T.; Ruoff, R. S. *Carbon* **2006**, *44*, 3342.
(57) Gao, X. H.; Wei, W. Z.; Yang, L.; Guo, M. L. *Electroanalysis* **2006**, *18*, 485.
(58) Pan, D. W.; Wang, Y. E.; Chen, Z. P.; Lou, T. T.; Qin, W. *Anal. Chem.* **2009**, *81*, 5088.
(59) Hwang, G. H.; Han, W. K.; Park, J. S.; Kang, S. G. *Talanta* **2008**, *76*, 301.
(60) Morton, J.; Havens, N.; Mugweru, A.; Wanekaya, A. K. *Electroanalysis* **2009**, *21*, 1597.
(61) Pan, D. W.; Wang, Y. E.; Chen, Z. P.; Yin, T. J.; Qin, W. *Electroanalysis* **2009**, *21*, 944.
(62) Liu, J.-F.; Zhao, Z.-S.; Jiang, G.-B. *Environ. Sci. Technol.* **2008**, *42*, 6949.